Contents lists available at ScienceDirect

Transactions of Nonferrous Metals Society of China

36(2026) 929−942

www.tnmsc.cn

Preparation and electrochemical performance of nitrogen-doped carbon-coated Cu_xS nanobox catalyst for hybrid Na−CO_2 batteries

Jing ZHAN [a,b,*], Zi-zhuo HUA [a], Fei-xiang WU [a,**], Qi-hou LI [a,***]

[a] School of Metallurgy and Environment, Central South University, Changsha 410083, China;

[b] School of New Energy and Mining, Xinjiang University of Technology, Hetian 848000，China

Abstract: To promote CO_2 redox kinetics on the cathode of hybrid sodium−carbon dioxide (Na−CO_2) batteries, hollow cubic CuS nanoboxes were encapsulated in polypyrrole and polydopamine by in situ polymerization of pyrrole and dopamine monomers, respectively, and coupled with high-temperature heat treatment to obtain nitrogen−carbon encapsulated Cu_xS@NC_{PPy} and Cu_xS@NC_{PDA} catalysts. The results show that the encapsulation of nitrogen-doped carbon not only increases the specific surface area and improves the electron affinity but also promotes the synergistic interaction between the CuS-based active species and the defect carbon, thus providing abundant active sites for CO_2 conversion. The electrochemical performances of the carbon-coated modified samples were all improved, especially the hybrid Na−CO_2 battery based on Cu_xS@NC_{PPy}, which showed a low voltage gap of 0.74 V at 0.1 mA/cm^2 and a high power density of 3.42 mW/cm^2.

Keywords: CO_2 reutilization; copper (I) sulfide catalyst; nitrogen-doped carbon; high power density; Na−CO_2 batteries

1 Introduction

Effectively addressing carbon emissions in key industries such as steel, petrochemicals, non-ferrous metals, and construction materials has become a global focal point of concern. Balancing the escalating global energy demand while economically mitigating carbon dioxide (CO_2) emissions stands out as a paramount challenge in contemporary time [1,2]. Specifically, the aluminum electrolysis industry, a crucial sector that produces substantial greenhouse gas emissions, is estimated to have average specific emissions ranging from 14 to 17 t of CO_2 per ton of aluminum produced, covering the entire process from bauxite mining to cast metal production [3]. Given the magnitude of these emissions, the industry is under increasing pressure to actively contribute to global emission reduction goals [4−6]. Therefore, to address this challenge and meet the dual-carbon strategy objectives of carbon peak and carbon neutrality, the urgent adoption of innovative technologies for CO_2 treatment is imperative.

Metal−carbon dioxide batteries not only incorporate CO_2 into the battery system providing an effective means of CO_2 utilization, but also serve as energy storage devices for intermittent renewable energy. This functionality enables them to supply ample electricity to meet daily energy demands, thereby reducing reliance on fossil fuels. Sodium−carbon dioxide (Na−CO_2) batteries, in particular, have gained favor due to the abundant and cost-effective nature of sodium resources and a theoretical energy density 1125 W·h/kg, surpassing that of lithium-ion batteries significantly [7−9].

Corresponding author: *Jing ZHAN, Tel: +86-13975147556, E-mail: zhanjing@csu.edu.cn;
**Fei-xiang WU, Tel: +86-13786154857, E-mail: feixiang.wu@csu.edu.cn;
***Qi-hou LI, Tel: +86-13975158738, E-mail: liqihou@csu.edu.cn

https://doi.org/10.1016/S1003-6326(25)67007-5

Received 16 January 2025; accepted 19 September 2025

Nonetheless, current Na−CO_2 batteries face problems such as large electrode polarization and poor reversibility, which mainly stem from the sluggish kinetics of CO_2 reduction reactions (CO_2RR) and carbonate decomposition reactions (CO_2ER) at the CO_2 cathode. In this regard, identifying suitable electrocatalysts to promote CO_2 redox kinetics is one of the most active research areas at present [10−12]. Extensive work has been carried out on the development of catalysts, including carbon materials [13,14], noble metals and their composites [15−17], transition metal oxides [18,19], and sulfur compounds [20,21]. Notably, transition metal sulfides have garnered considerable attention in the energy conversion field owing to their abundant availability, cost-effectiveness, and versatile design possibilities [22]. Nevertheless, it is noteworthy that metal sulfides still face challenges in practical applications, such as poor electrical conductivity and insufficient active sites. To fully unleash the catalytic potential, further modulation of material composition, morphology engineering, coating, or doping is required to enhance both electrical conductivity and catalytic activity [23−26]. For example, constructing conducting polymer-coated nanostructures for CO_2 cathode catalysts has been considered an effective strategy to enhance the performance of hybrid Na−CO_2 batteries due to the dimension/morphology and the synergistic effect of different components [27]. Particularly, polypyrrole (PPy) and polydopamine (PDA) are among the most widely studied conductive polymers in energy storage research, owing to their notable properties, including superior electrical conductivity, robust chemical stability, simple fabrication processes, and eco-friendly nature [27,28]. In addition, their derived nitrogen-doped carbons stand out due to their low cost, chemical stability, tunable conductivity, and electrochemical activity.

Based on the above considerations, a simple multi-step templating strategy was employed in this work to successfully prepare hollow cubic-shaped CuS nanobox catalysts. Further, by combining the encapsulation of PPy and PDA and heat treatment techniques, two nitrogen-doped carbon-coated nanoboxes, named $Cu_xS@NC_{PPy}$ and $Cu_xS@NC_{PDA}$, respectively, were successfully synthesized. The encapsulation of nitrogen-doped carbon appears to have positive effects on material properties, electron affinity, and the interaction between CuS-based active species and defect carbon. This, in turn, provides a great number of active sites for CO_2 conversion. As expected, the electrochemical properties of the carbon-coated modified samples were all improved. Especially, the hybrid Na−CO_2 battery based on $Cu_xS@NC_{PPy}$ showed a low voltage gap of 0.74 V at 0.1 mA/cm^2 and a high power density of 3.42 mW/cm^2. This work improves the performance of the catalyst through material design and modification, providing potential value for its application in CO_2 batteries.

2 Experimental

2.1 Catalyst synthesis

Without any additional purification, the target samples were prepared using the chemical reagents directly. The CuO/CuS catalysts were synthesized using a conventional method [28]. Initially, 1.5 g of $CuSO_4·5H_2O$ and 0.6 g of trisodium citrate were dissolved in 320 mL of deionized (DI) water to create Solution A. Subsequently, 4 g of NaOH was dissolved in 80 mL of DI water and added to Solution A. After stirring for 15 min, a 200 mL DI water solution containing 1.06 g of ascorbic acid was incorporated into Solution A, and the mixture was stirred for an additional hour. The resulting red product was filtered and washed with DI water and ethanol to yield Cu_2O nanoboxes. Secondly, the Cu_2O nanoboxes were dispersed in 240 mL of DI water to create Solution B. Next, 0.24 g of Na_2S was dissolved in 160 mL of DI water and added to Solution B. After stirring for 0.5 h, the mixture was filtered and thoroughly washed to yield Cu_2O/CuS nanoboxes. Thirdly, the prepared Cu_2O/CuS nanoboxes were dispersed in a mixed solvent of 80 mL of ethanol and 80 mL of H_2O to obtain Solution C. Subsequently, 10.2 g of $Na_2S_2O_3$ was dissolved in 64 mL of DI water and added to Solution C. After being stirred for 0.5 h, the mixture underwent filtration and thorough washing to yield hollow CuO/CuS nanoboxes.

Two methods were employed to prepare nitrogen-doped carbon-coated Cu_xS nanoboxes [27,28]. Method (1): 60 mg of CuO/CuS was first dispersed in 80 mL of deionized water, to which 12 mg of sodium dodecyl sulfate was added. After sonication for 0.5 h and stirring for 1 h, 60 μL of pyrrole was injected. Following an additional hour of stirring, 16 mL of 0.1 mol/L ammonium persulphate solution

was introduced. The mixture was stirred for 4 h, filtered, washed, and then dried at 80 °C overnight. Finally, the prepared sample was annealed in nitrogen at 550 °C for 2 h with a heating rate of 2 °C/min to obtain target catalysts, named $Cu_xS@NC_{PPy}$. Method (2): 60 mg of CuO/CuS nanoboxes and 60 mg of dopamine hydrochloride were dispersed into 100 mL of tris buffer solution (10 mmol/L, pH=8.5) and stirred for 5 h. After filtration, the product was cleaned and dried at 80 °C overnight. Finally, the $Cu_xS@NC_{PDA}$ catalyst was obtained using the same heat treatment process.

2.2 Physicochemical characterization

The crystal structure of all as-prepared samples and charge−discharge products was estimated through X-ray diffraction (XRD, Rigaku-TTRIII) with Cu K_α at a scan rate of 8(°)/min. The morphology of as-prepared samples was inspected with field-emission scanning electron microscopy (SEM, JSM−7900F) with an energy-dispersive X-ray analyzer (EDX). The Raman spectra were examined using an inVia Raman spectrometer. The nitrogen adsorption isotherms (Quantachrome Instruments) were utilized to determine the Brunauer−Emmett−Teller (BET) specific surface area. The determination of carbon content was conducted using thermogravimetry-differential thermal analysis (TG-DTA, NETZSCH STA 449F5). Relevant information regarding the chemical composition and surface chemical valence states of CuO/CuS, $Cu_xS@NC_{PPy,}$ and $Cu_xS@NC_{PDA}$ was analyzed using X-ray photoelectron spectroscopy (XPS, Thermo K-alpha).

2.3 Electrochemical measurement

The electrochemical characterization was conducted utilizing a custom-made hybrid Na−CO_2 battery mold. The working electrode was fabricated by coating commercial Toray carbon paper (1 cm of diameter) with a slurry comprising active material, conductive carbon, and 5 wt.% PTFE binder. The effective area of the cathode was 0.79 cm^2, with a mass loading of 2.0 mg/cm^2 of active material in this work. The anolyte consisted of 1 mol/L $NaClO_4$ solution dissolved in a mixture of dimethyl carbonate and ethylene carbonate (DMC/EC, 1∶1 by volume), with the addition of 1% fluorinated ethylene carbonate (FEC). Around 0.2 mL of a saturated solution of sodium chloride was utilized as the catholyte, while a $Na_3Zr_2Si_2PO_{12}$ solid electrolyte (NASICON) with a thickness of 1 mm and an effective area of 0.79 cm^2 was employed as the separator, and sodium metal foil served as the anode. The assembly of all batteries was conducted within a glove box environment featuring a water and oxygen content below 0.6×10^{-6}. The prepared batteries were enclosed in a container filled with pure CO_2 for conducting electrochemical performance measurements at room temperature. These measurements included charge/discharge voltages, galvanostatic intermittent titration technique (GITT), and rate performance assessments, which were performed using a LAND battery tester (CT2001A). Polarization curves and electrochemical impedance spectroscopy (EIS) spectra were obtained using a CHI 760e electrochemical workstation.

3 Result and discussion

3.1 Characteristics of CuO/CuS nanoboxes

The exquisite design of hollow CuO/CuS nanoboxes was achieved by meticulously customizing their morphology through a typically multi-step template-driven strategy [28], commencing with the utilization of a Cu_2O nanocube template and subsequently undergoing sequential sulfidation and etching processes. To gain a deep understanding of the CuO/CuS structuring process, the evolution of phases of the target samples at each stage was initially investigated via X-ray diffraction (XRD) and energy-dispersive X-ray analyzer (EDX). The template samples, as illustrated in Fig. 1(a), exhibit prominent peaks at approximately 29.6°, 36.4°, 42.3°, 52.5°, 61.4°, 73.5°, and 77.4°, respectively corresponding to the crystal planes (110), (111), (200), (211), (220), (311), and (222) of Cu_2O (PDF#78-2076). EDX analyses further indicate the phase purity of prepared Cu_2O nanocubes (Fig. 1(d)). When the Cu_2O nanocubes were immersed in an appropriate amount of Na_2S solution, a significant transformation was observed in Fig. 1(b), while the presence of S element was also confirmed by the EDX spectrum (Fig. 1(e)), thereby indicating the formation of CuS species on the surface of Cu_2O nanocubes. After selective etching of the Cu_2O inner core with sodium thiosulfate solution, the resulting products exhibited XRD spectra with diffraction peaks corresponding to CuS and CuO (Fig. 1(c)). Specifically, peaks observed at

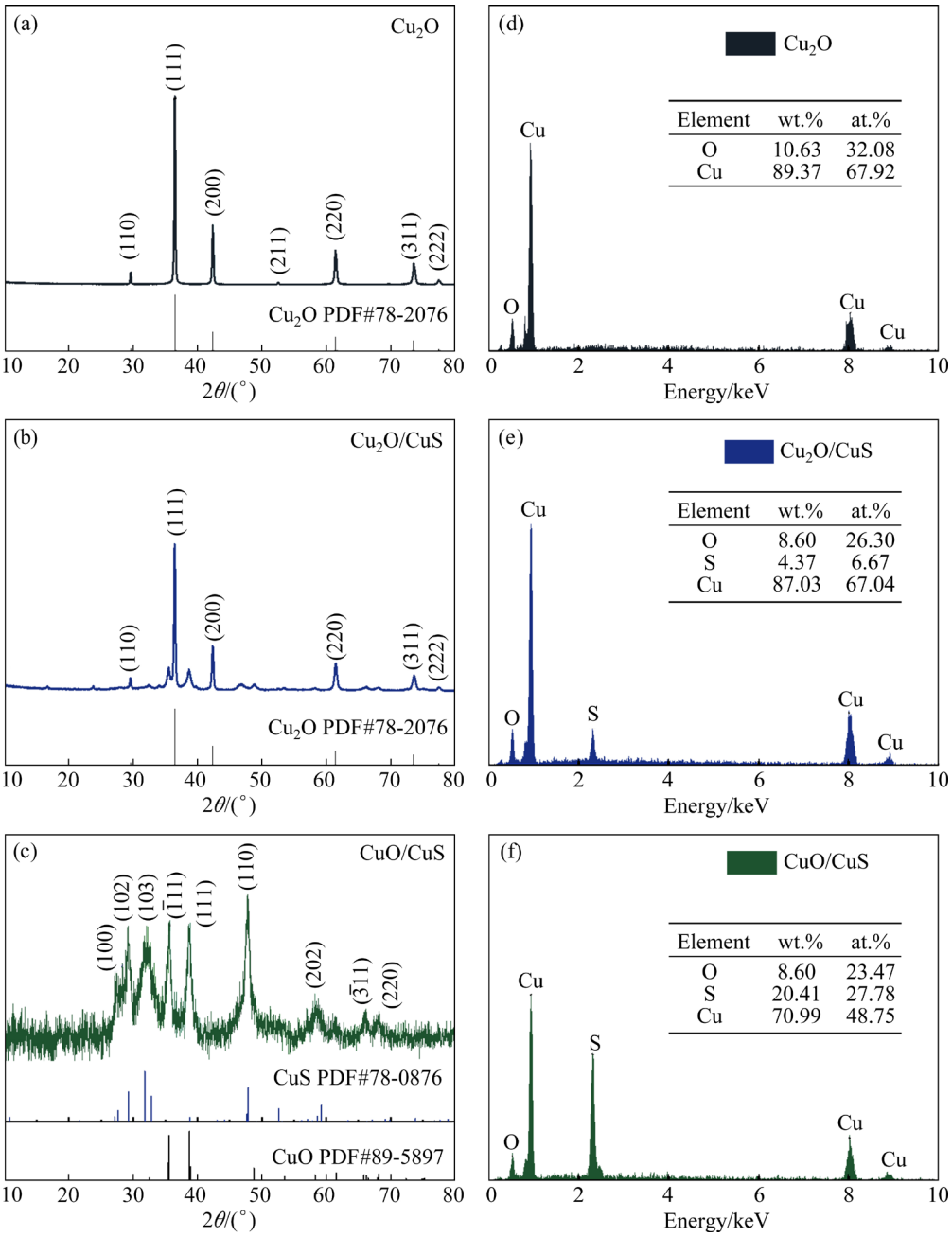

Fig. 1 XRD patterns (a−c) and EDX spectra (d−f) of Cu_2O, Cu_2O/CuS, and CuO/CuS nanoboxes

around 27.1°, 29.2°, 31.7°, and 47.9° corresponded to the crystal planes (100), (102), (103), and (110) of CuS (PDF#78-0876), respectively. In addition, the peaks detected at approximately 35.6°, 38.7°, 58.3°, 66.2°, and 68.1° were attributed to the crystal planes $(\bar{1}11)$, (111), (202), $(\bar{3}11)$, and (220) of CuO (PDF#89-5897), respectively. Furthermore, the elemental compositions of Cu, O, and S were further verified by EDX in Fig. 1(f).

The morphological evolution of the prepared samples was examined by scanning electron microscopy (SEM). SEM images at different magnifications demonstrate the uniformity, well-defined structure, and excellent consistency of the synthesized Cu_2O nanocubes, with a size of about 650 nm and a smooth surface (Figs. 2(a−c)). Following sulfidation, the SEM images of the Cu_2O nanocubes (Figs. 2(d−f)) reveal a significantly roughened surface, accompanied by the growth of a nanosheet shell, indicating the formation of Cu_2O/CuS core−shell nanocubes. The evidence presented in Figs. 2(g−i) indicates the successful formation of hollow nanobox structures in CuO/CuS samples through selective etching.

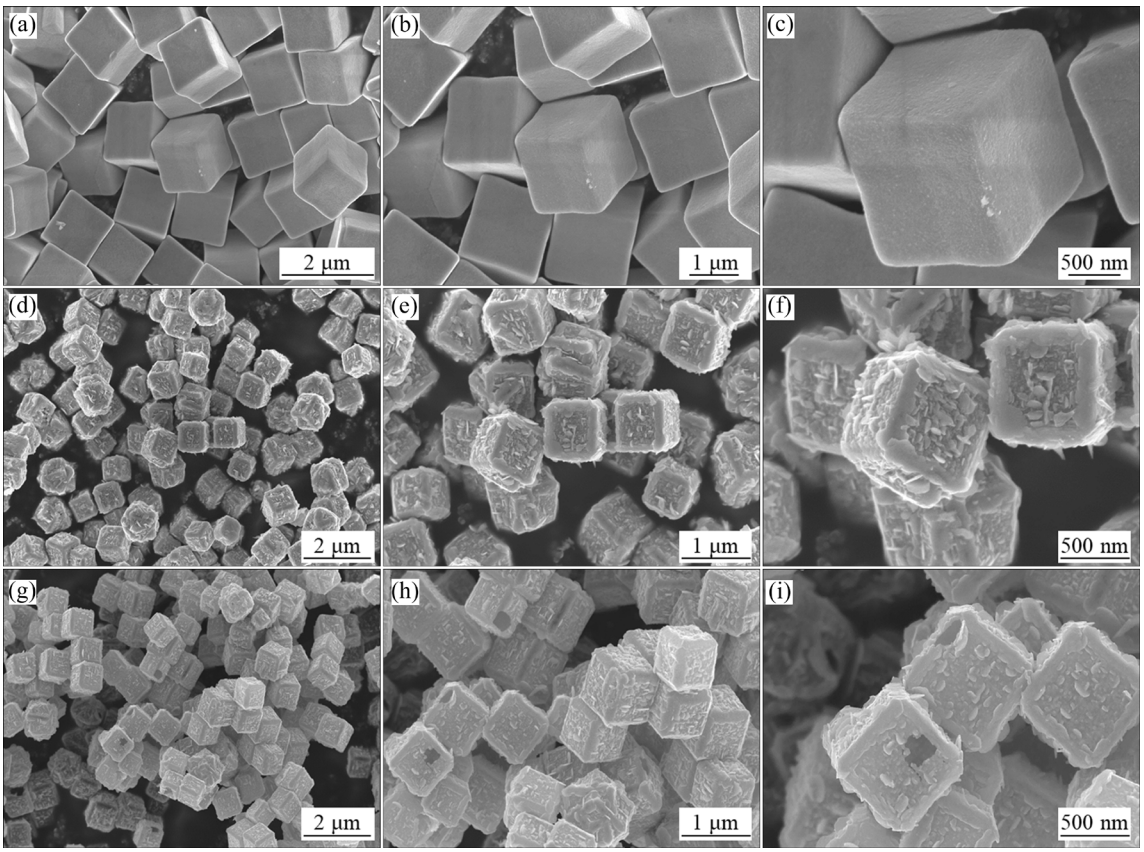

Fig. 2 FESEM images of Cu_2O (a−c), Cu_2O/CuS (d−f), and CuO/CuS (g−i) nanoboxes

3.2 Characteristics of nitrogen-doped carbon-coated Cu_xS nanobox

The crystal structures and purity of the as-prepared nitrogen-doped carbon-coated Cu_xS nanobox samples were analyzed in Fig. 3. For the $Cu_xS@NC_{PPy}$ sample (Fig. 3(a)), the peaks located at 27.7°, 32.1°, 46.1°, and 54.6° are noticed, respectively corresponding to (111), (200), (220), and (222) lattice planes, which are matched well with $Cu_{1.95}S$ (PDF#89-2072). Moreover, the peaks located at 32.6° and 39.0° correspond to the (111)/ (103) and (104) lattice planes of Cu_2S (PDF#72-1071). However, the phase of $Cu_xS@NC_{PDA}$ is different from that of $Cu_xS@NC_{PPy}$. As we can see from the XRD pattern of $Cu_xS@NC_{PDA}$ in Fig. 3(b)), most of the diffraction peaks correspond to $Cu_{1.96}S$ (PDF#29-0578). The discernible peaks at 36.4°, 42.3°, 61.4°, and 73.5° align with the (111), (200), (220), and (311) lattice planes of Cu_2O (PDF#99-0041), respectively. This observation can be attributed to the reduction of CuO during the elevated temperature treatment. The EDX analyses in Figs. 3(c) and (d) unequivocally validate the achievement of nitrogen-doped carbon encapsulation, wherein the nitrogen-doped carbon content within $Cu_xS@NC_{PPy}$ surpasses that observed in $Cu_xS@NC_{PDA}$. This pronounced disparity underscores the superior nitrogen-doping efficacy and encapsulation performance inherent in the $Cu_xS@NC_{PPy}$ composite in this work. A high nitrogen-doped carbon content typically exerts a positive influence on catalytic performance, owing to its ability to enhance electron conductivity, introduce active sites, and alter the selectivity and reaction kinetics of the catalyst [29].

Morphologies of $Cu_xS@NC_{PPy}$ and $Cu_xS@NC_{PDA}$ samples were also further examined to validate the presence of nitrogen-doped carbon coating on their structures. As demonstrated in Fig. 4, the products obtained through the application of two distinct methods manifest a pronounced inheritance of the morphological structure from CuO/CuS nanoboxes. Additionally, a conspicuous presence of the nitrogen-doped carbon coating layer is distinctly visible, highlighting the effectiveness of the encapsulation process. It is noted that a large number of nanoparticles are also present on the surface of the $Cu_xS@NC_{PPy}$ sample, primarily originating from polypyrrole-induced nitrogen-doped carbon formation.

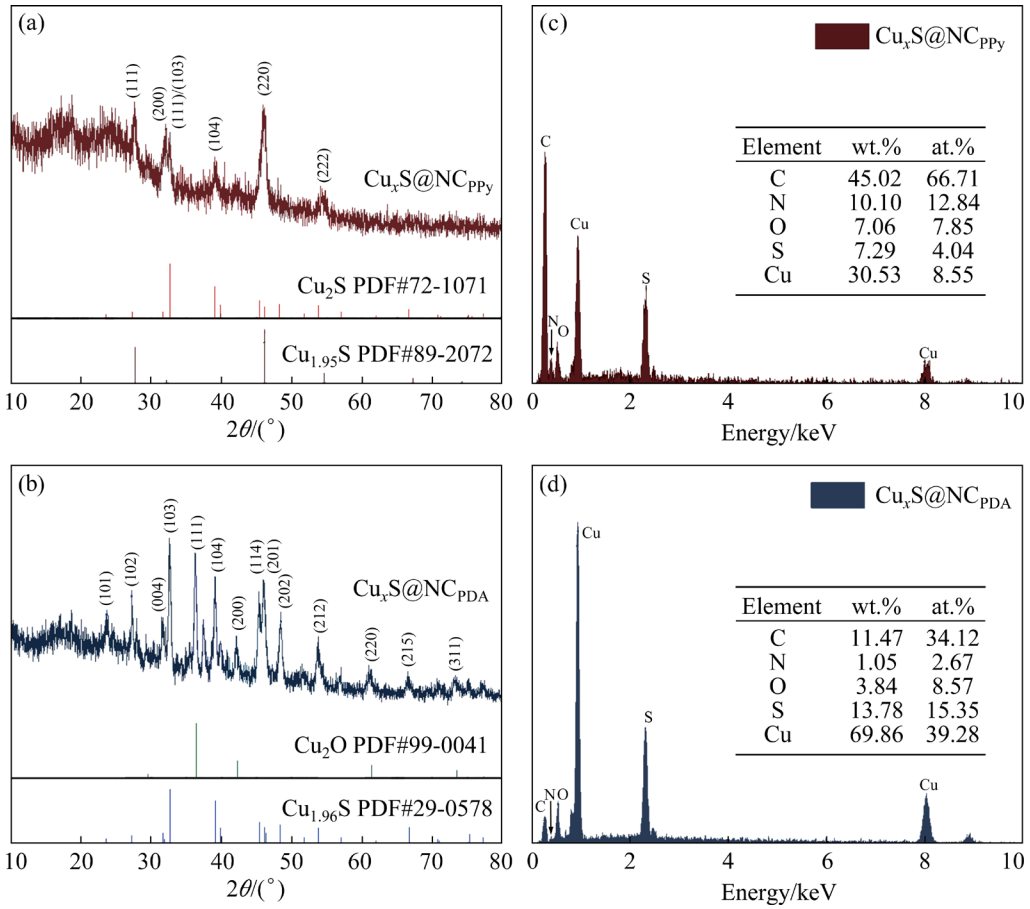

Fig. 3 XRD patterns (a, b) and EDX spectra (c, d) of $Cu_xS@NC_{PPy}$ and $Cu_xS@NC_{PDA}$ nanoboxes

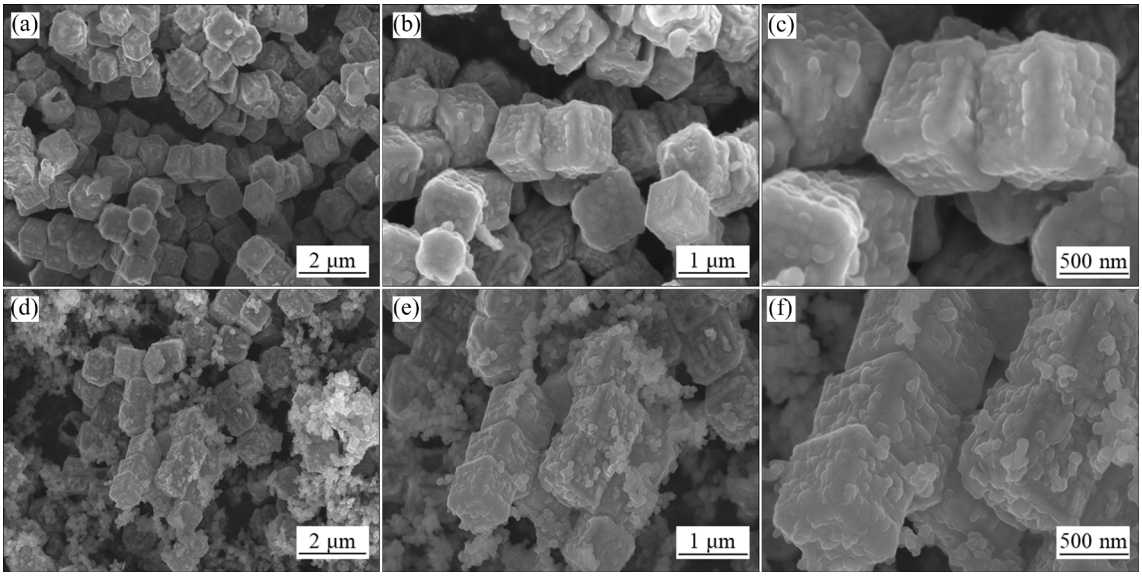

Fig. 4 FESEM images of $Cu_xS@NC_{PDA}$ (a−c) and $Cu_xS@NC_{PPy}$ (d−f) nanoboxes

To accurately evaluate the effectiveness of both methods in producing carbon coatings, we conducted thermogravimetry-differential thermal analysis (TG−DTA) tests in an ambient air environment, as illustrated in Fig. 5. The samples were subjected to a heating rate of 10 °C/min, gradually reaching a temperature of 900 °C. Observations from Fig. 5(a) reveal a significant increase in the TG curve of CuS/CuO at approximately 268.5 °C, followed by a declining trend after 600 °C. The corresponding

DTA curve exhibits distinct endothermic and exothermic peaks, primarily associated with phase transitions among oxides (Cu_2O and/or CuO), sulfides (Cu_xS), and sulfate species ($CuSO_4$, $CuO·CuSO_4$) [30]. $Cu_xS@NC_{PDA}$ exhibits a trend consistent with CuS/CuO, while $Cu_xS@NC_{PPy}$ shows markedly different behavior, attributed to a higher mass loss during the carbon removal stage compared to the increase due to copper−sulfur phase transitions. In $Cu_xS@NC_{PPy}$ samples, two main mass loss stages correspond to the removal of carbon and sulfur, with sulfate decomposition culminating in the production of CuO at temperatures exceeding 800 °C. The final residual mass fractions are 87.7% for CuS/CuO, 82.9% for $Cu_xS@NC_{PDA}$, and 22.3% for $Cu_xS@NC_{PPy}$, unequivocally demonstrating a higher carbon content in $Cu_xS@NC_{PPy}$ compared to $Cu_xS@NC_{PDA}$. The nitrogen adsorption−desorption isotherm curves of all samples are also investigated, as illustrated in Figs. 5(d−f). Based on the isotherms, all of which exhibit typical Type IV characteristics and pore size distribution curves, both indicating the predominant presence of a substantial quantity of mesopores. Notably, the largest specific surface area of $Cu_xS@NC_{PPy}$ (51.1 m^2/g) is revealed, larger than that of $Cu_xS@NC_{PDA}$ (23.7 m^2/g) and CuS (19.6 m^2/g). The enhanced high specific surface area and mesoporous structure provide several advantages for

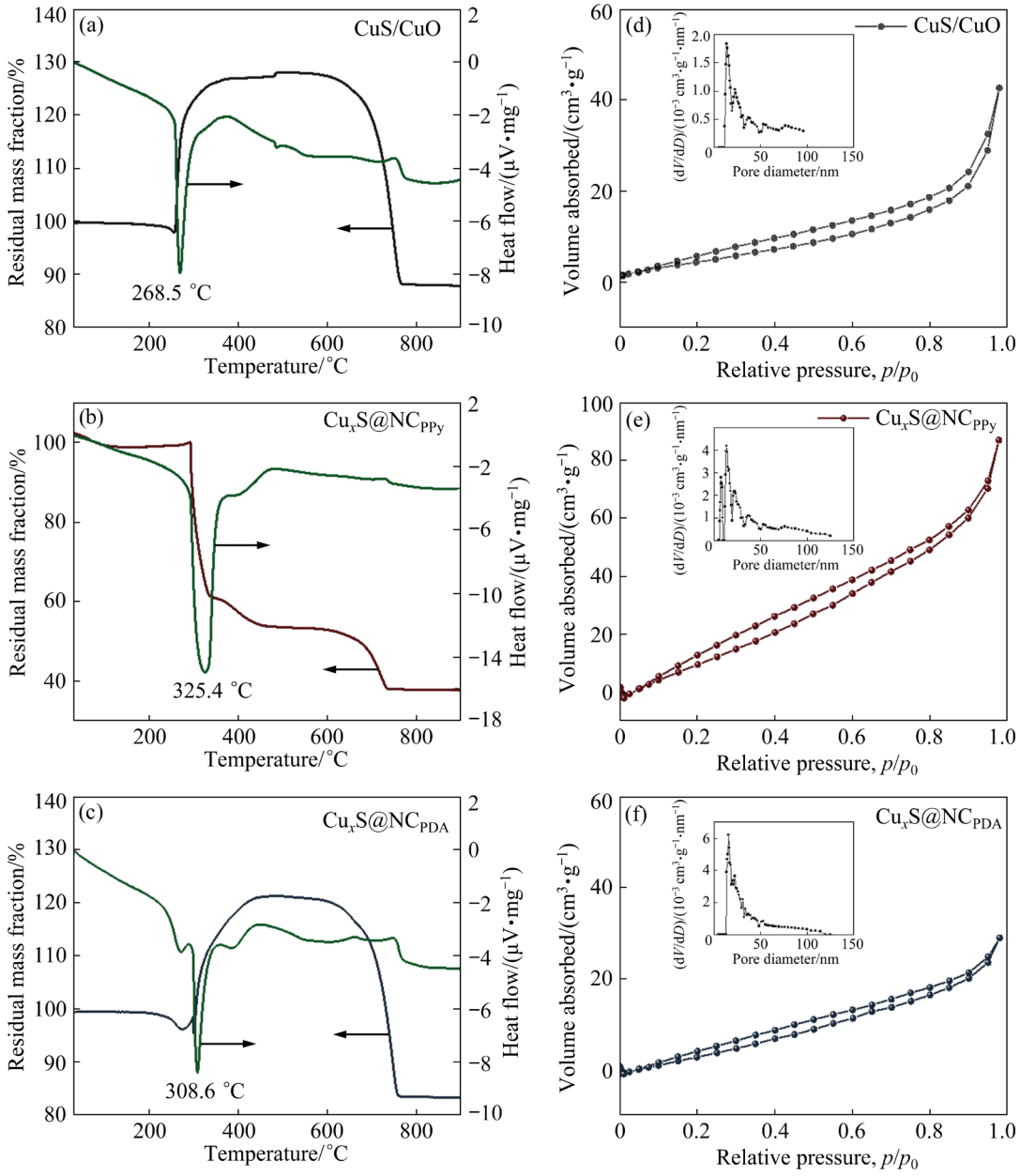

Fig. 5 TG−DTA curves (a−c) and nitrogen adsorption−desorption isotherms and pore size distribution curves (d−f) of CuS/CuO, $Cu_xS@NC_{PPy}$ and $Cu_xS@NC_{PDA}$ nanoboxes

CO_2RR and CO_2ER [13,21]. For example, the high specific surface area provides more active sites, increasing the opportunity for CO_2 adsorption and reaction, while the mesoporous structure provides channels for the penetration of CO_2 and electrolyte, ensuring the effective diffusion of reactants on the catalyst surface, which is expected to reduce the polarization generated by the charge−discharge reaction.

X-ray photoelectron spectroscopy (XPS) was utilized to investigate the surface elemental composition and valence states of CuS/CuO, $Cu_xS@NC_{PPy}$, and $Cu_xS@NC_{PDA}$ samples. As anticipated, distinct signals corresponding to Cu 2p, O 1s, N 1s, C 1s, and S 1s are evident, respectively at approximately 932, 531, 399, 284, and 161 eV in the survey spectra of $Cu_xS@NC_{PPy}$ and $CuxS@NC_{PDA}$ (Fig. 6(a)). The survey spectrum of CuS/CuO does not reveal any discernible peak associated with the N element. The high-resolution deconvoluted XPS Cu 2p spectra reveal intriguing features, as illustrated in Fig. 6(b). For the Cu 2p spectrum of CuS/CuO, a distinctive double peak emerges at 932.2 and 934.1 eV, along with a second double peak at 952.3 and 954.6 eV, corresponding to the Cu $2p_{3/2}$ and Cu $2p_{1/2}$ core levels, respectively [31]. Specifically, the peaks at 932.2 and 934.1 eV are associated with Cu(I) and Cu(II) states. Additionally, distinctive oscillatory satellite peaks are observed at 942.1 and 944.3 eV, providing evidence for the presence of copper ions in the Cu^{2+} oxidation state [27]. In the $Cu_xS@NC_{PPy}$ sample, the peaks associated with Cu(II) and satellite peaks noticeably decrease, indicating that a significant amount of Cu(II) is reduced to Cu(I) during the subsequent carbon coating process. Notably, in the $Cu_xS@NC_{PDA}$ sample, the presence of peaks associated with Cu(II) is nearly negligible. Furthermore, distinct peak shifts towards lower binding energies were detected in both the $Cu_xS@NC_{PPy}$ and $Cu_xS@NC_{PDA}$ samples, indicating the formation of copper species in lower oxidation states.

In the case of deconvoluted S 2p spectra (Fig. 6(c)), the peaks at binding energies of around 162 and 163 eV could be attributed to the $2p_{3/2}$ and $2p_{1/2}$ core levels of S^{2-}, respectively, primarily arising from CuS or Cu_xS [32,33]. Meanwhile, the peaks at 164 and 165.1 eV in the spectra were attributed to the $2p_{3/2}$ and $2p_{1/2}$ of S atoms in C—S—C and C═S, respectively, which mainly originated from the incorporation of S into the carbon skeleton by the thermal treatment process to form the C—S bonding groups. The existence of the C—S bonds, which have been recognized as an effective active site, contributes to considerable catalytic activity [32]. Notably, a significant shift of the centered peak toward higher binding energy is observed in $Cu_xS@NC_{PPy}$, indicating the presence of a significant amount of sulfur-doped carbon. The peak at around 168 eV was assigned to the oxidized S species, labeled as SO_x^{n-}, indicating the presence of some sulfate/sulfite moieties in the materials [33,34].

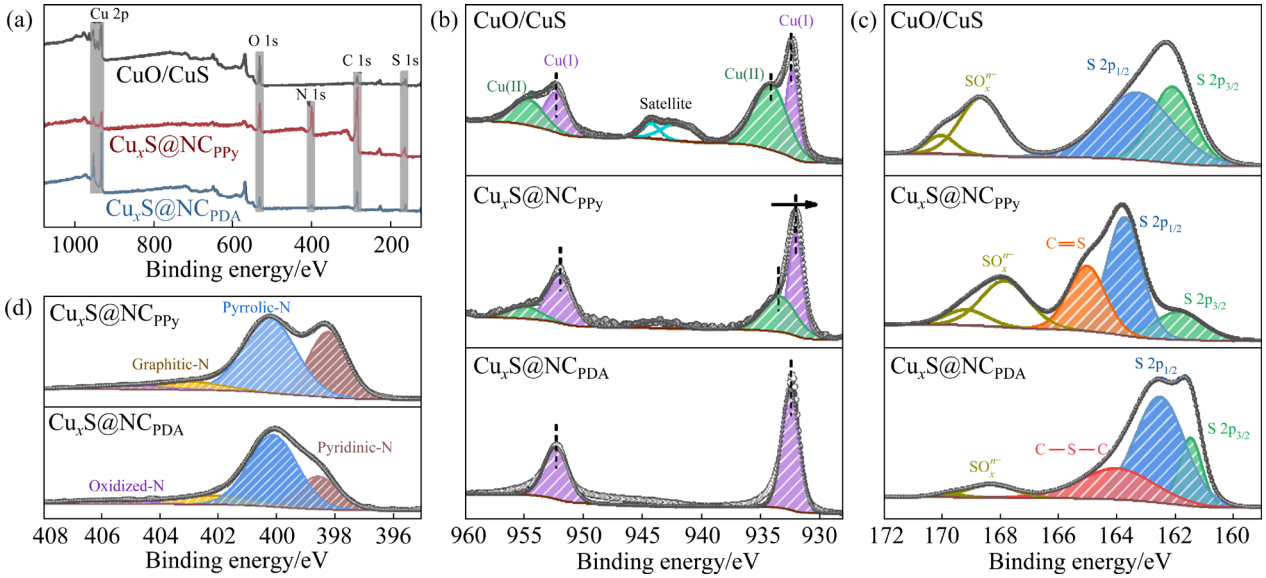

Fig. 6 Analysis of valence state on surface for CuS/CuO, $Cu_xS@NC_{PPy}$, and $Cu_xS@NC_{PDA}$: (a) Full XPS spectra; (b−d) High-resolution XPS spectra of Cu 2p, S 2p and N 1s, respectively

In the case of the high-resolution XPS spectra of N 1s of the $Cu_xS@NC_{PPy}$ and $Cu_xS@NC_{PDA}$ materials (Fig. 6(d)), four main peaks associated with pyridinic-N (398.4 eV), pyrrolic-N (400.2 eV), graphitic-N (402.6 eV), and oxidized-N (403−406 eV) species were observed. The overall nitrogen contents based on the XPS results of $Cu_xS@NC_{PPy}$ and $Cu_xS@NC_{PDA}$ are 14.0% and 5.6%, respectively. Typically, a substantial nitrogen doping level is known to introduce extra electrons, allowing for the modulation of the catalyst's electronic structure. Specifically, pyridinic-N and pyrrolic-N can serve as efficient active sites, potentially facilitating the progress of CO_2RR and CO_2ER [13].

As shown in Fig. 7, the Raman spectra were also carried out to confirm the encapsulation of carbon. Notably, there are two distinct bands at ~1360 and ~1580 cm^{-1} in the spectra of $Cu_xS@NC_{PPy}$ and $Cu_xS@NC_{PDA}$. The first band is indexed to D-bands (disorder-induced phonon mode), while another is assigned to G-bands (graphite band) of carbon [5]. The I_D/I_G ratio (where I_D and I_G represent the Raman intensities of the D-band and G-band, respectively) is commonly utilized to assess the degree of defects/disordered carbon and graphitization/ordered carbon in synthesized carbon materials [5,21,35]. The I_D/I_G ratios for $Cu_xS@NC_{PPy}$ and $Cu_xS@NC_{PDA}$ are 0.97 and 0.98, respectively, revealing the presence of numerous defect sites and structural distortions in the materials. This is highly advantageous for enhancing the electrocatalytic performance through increasing CO_2 adsorption capacity.

3.3 Electrocatalyst performance of hybrid Na−CO_2 battery

The obtained nitrogen-doped carbon-coated CuO/CuS nanoboxes, as revealed by the aforementioned results and analysis, exhibit promising prospects as catalysts for hybrid Na−CO_2 batteries. To assess the practical electrocatalytic performance of the synthesized samples, we assembled custom-made hybrid Na−CO_2 batteries for electrochemical testing, as depicted in Fig. 8(a). The hybrid Na−CO_2 battery utilized sodium foil as the anode and carbon paper loaded with the target catalyst as the CO_2 cathode, respectively. The intricate mechanisms underlying the battery reactions have been extensively deliberated upon in our previous works [21,36], with the corresponding

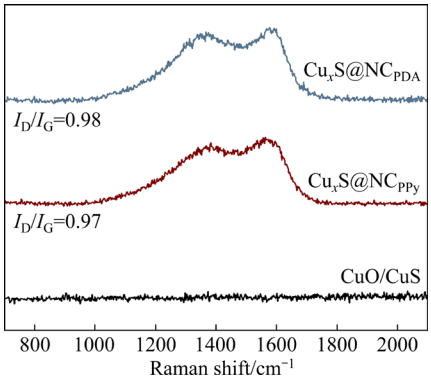

Fig. 7 Raman spectra of CuS/CuO, $Cu_xS@NC_{PPy}$ and $Cu_xS@NC_{PDA}$

reactions as

Anode:

$$4Na \rightleftharpoons 4Na^+ + 4e \quad (1)$$

Cathode:

$$4Na^+ + 3CO_2 + 4e \rightleftharpoons 2Na_2CO_3 + C \quad (2)$$

Overall:

$$4Na + 3CO_2 \rightleftharpoons 2Na_2CO_3 + C \ (E^{\ominus} = 2.35\ V) \quad (3)$$

$$Na_2CO_3 + CO_2 + H_2O \rightarrow 2NaHCO_3 \quad (4)$$

The voltage curves of batteries based on three catalysts were obtained at 0.1 mA/cm^2, as depicted in Fig. 8(b). The ultimate discharge and charging voltages of the battery using the CuO/CuS catalyst were 1.75 and 2.76 V, respectively, leading to a 1.01 V charge−discharge voltage gap. Owing to the nitrogen−carbon encapsulation, the battery with $Cu_xS@NC_{PDA}$ catalyst showed a slightly better performance with a discharge voltage of 1.8 V and a charge voltage of 2.69 V, bringing about a charge−discharge voltage gap of 0.89 V. The excitement that the battery with $Cu_xS@NC_{PPy}$ catalyst led to a greater discharge voltage of 1.91 V and a smaller charge voltage of 2.65 V, with an ultra-low voltage gap of only 0.74 V. What is more, the corresponding round-trip efficiencies of these batteries with CuO/CuS, $Cu_xS@NC_{PDA}$, and $Cu_xS@NC_{PPy}$ catalysts were calculated to be 63.47%, 66.9%, and 72.1%, respectively, indicating the outstanding charge−discharge catalytic activity of $Cu_xS@NC_{PPy}$ catalyst. Remarkably, these batteries obtained low charging voltage (<3 V), especially the battery with $Cu_xS@NC_{PPy}$, arising not only from the enhanced reaction kinetics of hybrid Na−CO_2 batteries because of soluble discharge products [36], but also from the interaction of numerous catalytic active species in $Cu_xS@NC_{PPy}$ for accelerating discharge product decomposition.

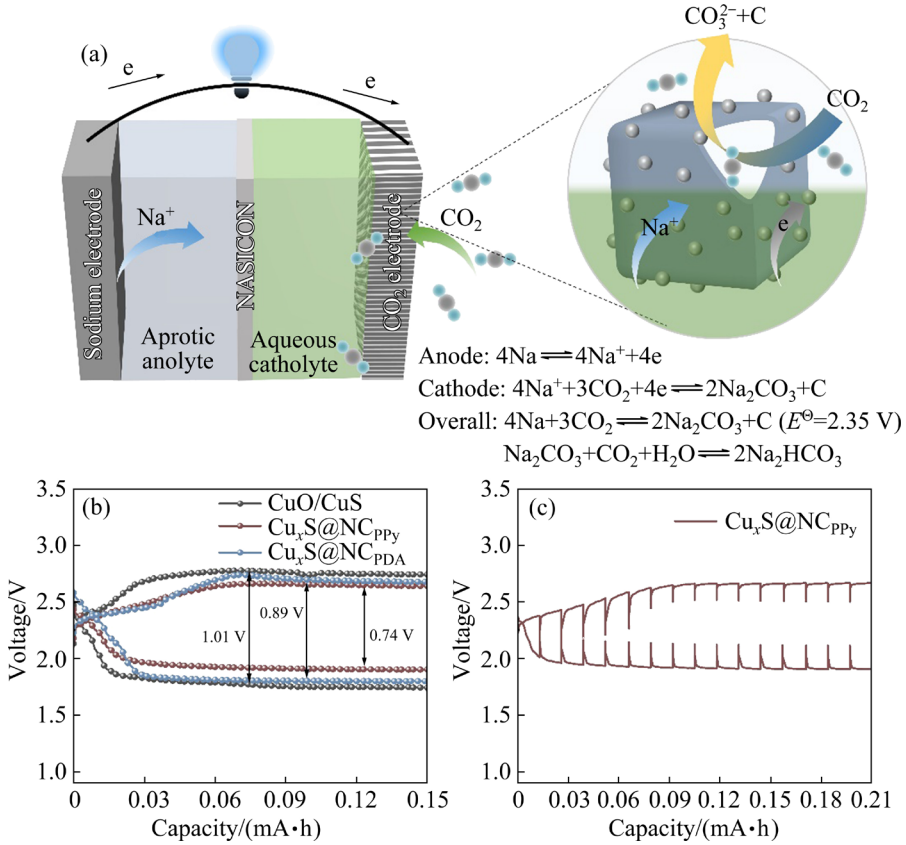

Fig. 8 Schematic of hybrid Na−CO_2 battery system (a), discharge−charge voltage curves at current density of 0.1 mA/cm^2 (b), and GITT curve of Cu_xS@NC_{PPy} (c)

To further investigate the catalytic activity of Cu_xS@NC_{PPy} in a hybrid Na−CO_2 battery, the galvanostatic intermittent titration technique (GITT) was employed to eliminate the concentration polarization induced by Na^+ and CO_2 diffusion, focusing solely on investigating the activation polarization of Cu_xS@NC_{PPy}. The GITT program was set as follows: at a current density of 0.1 mA/cm^2, the battery underwent a discharge or recharge cycle for 10 min followed by a resting period of 10 min to restore the battery voltage to its steady-state equilibrium [13,37]. As illustrated in Fig. 8(c), batteries utilizing the Cu_xS@NC_{PPy} catalyst exhibit a discharge equilibrium potential of 2.11 V and a charge equilibrium potential of 2.53 V, closely aligning with the theoretical voltage ($E^\ominus$) of 2.35 V associated with Na_2CO_3 formation, thereby indicating adherence to the cell reaction mechanism. Additionally, analysis of the GITT curve reveals that both the discharge voltage plateau (1.91 V) and charge voltage plateau (2.66 V) remain consistent with constant current charge−discharge curves depicted in Fig. 8(b), affirming the stability of Cu_xS@NC_{PPy}.

The rate capability of hybrid Na−CO_2 batteries employing three different catalysts was further assessed under varying current densities. Figure 9(a) illustrates the decrease in discharge voltage with increasing current density for the three active materials over the entire range of current densities investigated in this study. As depicted in Fig. 9(b), the battery with the Cu_xS@NC_{PPy} catalyst exhibits higher discharge voltages compared to those with Cu_xS@NC_{PDA} and CuO/CuS catalysts, particularly at high current densities. Even at a high current density of 1.0 mA/cm^2, the discharge voltage of the battery with the Cu_xS@NC_{PPy} catalyst (1.36 V) remains superior to that of Cu_xS@NC_{PDA} (1.22 V) and CuO/CuS (1.18 V) catalysts. The rate capability of the catalysts is enhanced after carbon coating, primarily due to the improved conductivity. Among these catalysts, Cu_xS@NC_{PPy} demonstrated the most significant rate performance, attributed to its superior carbon coating, providing enhanced conductivity, high surface area, and abundant defects to facilitate electron and mass transfer, offering numerous catalytic active sites.

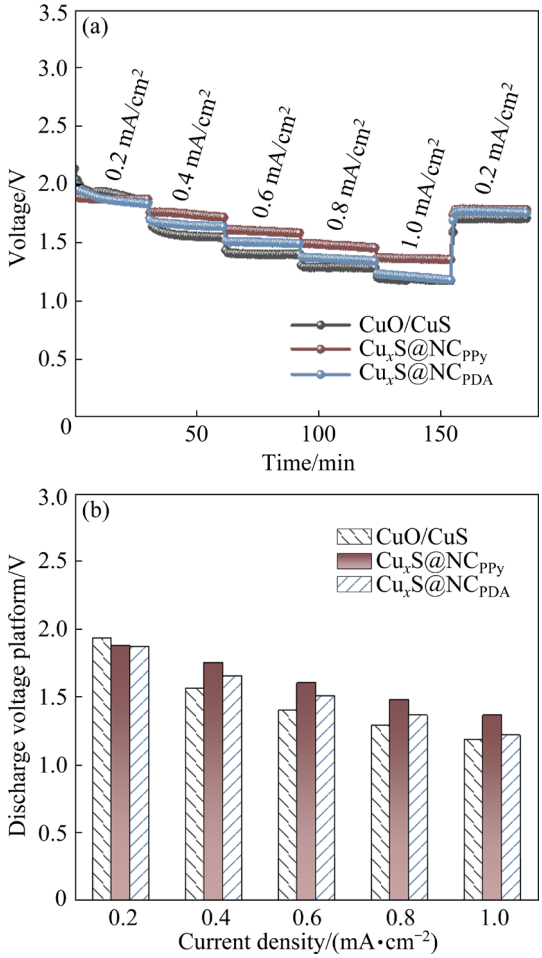

Fig. 9 Discharge voltage profiles (a) and discharge voltage platform (b) of hybrid Na−CO_2 battery with various catalysts at different current densities

The electrochemical characteristics enhanced by the three catalysts were further investigated through an electrochemical impedance spectroscopy (EIS) analysis, as illustrated in Fig. 10. To assess the electrochemical resistance between the electrode and electrolyte, a simplified interface model associated with the corresponding equivalent circuit was proposed. The corresponding equivalent circuit model is illustrated in the inset of Fig. 10(a), and the impedance values for each component after fitting are listed in Table 1. In this model, the low-frequency linear segment corresponds to CO_2 diffusion impedance (Z_w), the medium-frequency large semicircle corresponds to charge transfer resistance in the CO_2 electrode (R_{ct}), and the resistance of the solid electrolyte interface (SEI) film on the sodium metal surface (R_s). The high-frequency semicircle corresponds to the interface resistance (R_i), including the grain boundary resistance of the NASICON ceramic separator, as well as the interface resistance between the NASICON ceramic separator and the non-aqueous anolyte and aqueous catholyte. The intersection of the high-frequency real axis with the semicircle corresponds to the overall resistance of the electrode, NASICON, and electrolyte (R_e) [36,38,39]. The results presented in Fig. 10(a) and Table 1 demonstrate that the battery employing the Cu_xS@NC_{PPy} catalyst not only exhibits the smallest charge transfer resistance (R_{ct} ~3.6 Ω) but also possesses a lower total resistance (~284.2 Ω) compared to batteries with Cu_xS@NC_{PDA} catalyst (~358.7 Ω) or CuO/CuS catalyst (~475.0 Ω). These findings indicate that the utilization of the Cu_xS@NC_{PPy} catalyst showcases superior electron conductivity, effectively promoting charge transfer kinetics and enhancing reaction rates.

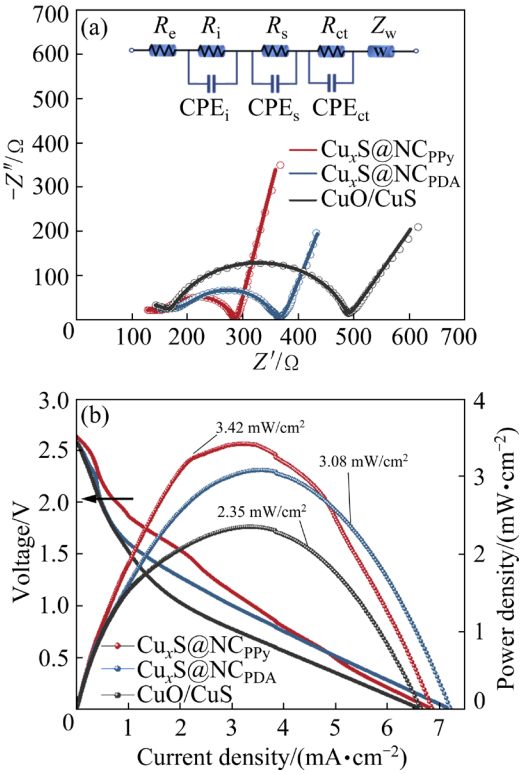

Fig. 10 EIS analysis and relative equivalent-circuit diagram (a), and discharge polarization and corresponding power density curves (b)

Table 1 Estimated elemental resistances in equivalent circuit

Sample	R_e/Ω	R_i/Ω	R_s/Ω	R_{ct}/Ω	Z_w/Ω
CuO/CuS	76.01	93.03	278.6	27.26	47.27
Cu_xS@NC_{PPy}	52.29	100.9	127.4	3.618	23.08
Cu_xS@NC_{PDA}	61.92	149.2	143.1	4.482	48.49

The catalytic efficacy of the three catalysts was evaluated by analyzing polarization curves with a scanning voltage rate of 5 mV/s. As illustrated in Fig. 10(b), the open-circuit voltage of the battery employing the $Cu_xS@NC_{PPy}$ catalyst exceeded that of the other two samples, resulting in a final current density of 6.84 mA/cm^2. Furthermore, the power density achieved by the battery utilizing the $Cu_xS@NC_{PPy}$ catalyst reached 3.42 mW/cm^2, demonstrating its superiority over batteries using either $Cu_xS@NC_{PDA}$ catalyst (3.08 mW/cm^2) or CuO/CuS catalyst (2.35 mW/cm^2). Batteries incorporating $Cu_xS@NC_{PPy}$ and $Cu_xS@NC_{PDA}$ catalysts exhibited smoother polarization curves and significantly higher current and power densities compared to those with CuO/CuS catalysts, underscoring an improvement in electrical conductivity facilitated by nitrogen-doped carbon-coated catalysts, thereby promoting catalytic activity. Unfortunately, the power density of these batteries was relatively low, primarily due to the high resistance components R_s and R_i, as shown in Fig. 10(a) and Table 1. This limitation could potentially be mitigated by introducing a highly conductive NASICON electrolyte and employing a liquid anode design.

4 Conclusions

(1) Two nitrogen-doped carbon-coated CuO/CuS nanoboxes, denoted as $Cu_xS@NC_{PPy}$ and $Cu_xS@NC_{PDA}$ nanoboxes, were synthesized employing a systematic multi-step templating approach integrated with polypyrrole and polydopamine encapsulation techniques.

(2) Nitrogen-doped carbon encapsulation significantly improves the conductivity of CuO/CuS materials and achieves a synergistic interaction between Cu-based active species and carbon defects, providing abundant active sites for CO_2 conversion.

(3) As cathode catalysts for hybrid Na−CO_2 batteries, both carbon-coated modified samples show enhanced electrochemical performance. Among them, $Cu_xS@NC_{PPy}$ shows the best performance with a low voltage gap (only ~0.74 V), round-trip efficiency of 72.1%, and a power density of 3.42 mW/cm^2. These results highlight the potential value of our designed materials for electrochemical applications, providing strong support for efficient CO_2 conversion.

CRediT authorship contribution statement

Jing ZHAN: Conceptualization, Investigation, Writing − Review & editing, Funding acquisition; **Zi-zhuo HUA:** Methodology, Data curation, Writing − Original draft; **Fei-xiang WU:** Supervision, Writing − Review & editing; **Qi-hou LI:** Supervision, Writing − Review & editing.

Declaration of competing interest

The authors declare that they have no known competing financial interests or personal relationships that could have appeared to influence the work reported in this paper.

Acknowledgments

This work was financially supported by the National Natural Science Foundation of China (No. 52172264), and the National Key Research and Development Program of China (No. 2022YFC3900802).

References

[1] ZHAN Jing, WANG Huan-wei, LI Qi-hou, WANG Zhi-jian, FANG Xin. Preparation of sillenite-type $Bi_{12}MnO_{20}$ with enhanced photocatalytic activity for removal of organic pollutants via superoxide radicals [J]. Transactions of Nonferrous Metals Society of China, 2023, 33(11): 3570−3582.

[2] XU Chang-fan, DONG Yu-lian, ZHAO Hua-ping, LEI Yong. CO_2 conversion toward real-world applications: Electrocatalysis versus CO_2 batteries [J]. Advanced Functional Materials, 2023, 33(32): 2300926.

[3] SAEVARSDOTTIR G, PADAMATA S K, VELASQUEZ B N, KVANDE H. The way towards zero carbon emissions in aluminum electrolysis [C]//Light Metals 2023. Cham: Springer, 2023: 637−645.

[4] YANG Yi, GUO Yao-qi, ZHU Wen-song, HUANG Jian-bai. Environmental impact assessment of China's primary aluminum based on life cycle assessment [J]. Transactions of Nonferrous Metals Society of China, 2019, 29(8): 1784−1792.

[5] PACHFULE P, SHINDE D, MAJUMDER M, XU Qiang. Fabrication of carbon nanorods and graphene nanoribbons from a metal−organic framework [J]. Nature Chemistry, 2016, 8(7): 718−724.

[6] HONG Ping, XU Chang-fan, YAN Cheng-zhan, DONG Yu-lian, ZHAO Hua-ping, LEI Yong. Prussian blue and its analogues for commercializing fast-charging sodium/potassium-ion batteries [J]. ACS Energy Letters, 2025, 10: 750−778.

[7] XU Chang-fan, DONG Yu-lian, SHEN Yong-long, ZHAO Hua-ping, LI Li-qiang, SHAO Guo-sheng, LEI Yong. Fundamental understanding of nonaqueous and hybrid Na−CO_2 batteries: Challenges and perspectives [J]. Small, 2023, 19(15): 2206445.

[8] XU Chang-fan, HONG Ping, DONG Yu-lian, ROBERT M,

SHAO Guo-sheng, LEI Yong. Toward complete CO_2 electroconversion: Status, challenges, and perspectives [J]. Advanced Energy Materials, 2026, 16: 2406146.

[9] XU Chang-fan, FANG Xin, ZHAN Jing, CHEN Jia-xi, LIANG Feng. Progress for metal−CO_2 batteries: Mechanism and advanced materials [J]. Progress in Chemistry, 2020, 32(6): 836−850.

[10] SARKAR A, DHARMARAJ V R, YI Chia-hui, IPUTERA K, HUANG Shang-yang, CHUNG Ren-jei, HU Shu-fen, LIU Ru-shi. Recent advances in rechargeable metal−CO_2 batteries with nonaqueous electrolytes [J]. Chemical Reviews, 2023, 123(15): 9497−9564.

[11] DONG Yu-lian, XU Chang-fan, FU Yong-huan, ZHAO Hua-ping, LEI Yong. Catalyzed carbon-based materials for CO_2−battery utilization [J]. Energy Materials, 2025, 5(4): 500039.

[12] YANG Xie-cheng, ZHANG Dan-tong, ZHAO Lan-qing, PENG Chao, REN Kun, XU Chang-fan, LIU Pan, ZHOU Ying-jie, LEI Yong, YANG Bin, XUE Dong-feng, LIANG Feng. Upgrading cycling stability and capability of hybrid Na-CO_2 batteries via tailoring reaction environment for efficient conversion CO_2 to HCOOH [J]. Advanced Energy Materials, 2024, 14(16): 2304365.

[13] XU Chang-fan, ZHAN Jing, WANG Huan-wei, KANG Yao, LIANG Feng. Dense binary Fe−Cu sites promoting CO_2 utilization enable highly reversible hybrid Na−CO_2 batteries [J]. Journal of Materials Chemistry A, 2021, 9(38): 22114−22128.

[14] HU Xiao-fei, SUN Jian-chao, LI Zi-fan, ZHAO Qing, CHEN Cheng-cheng, CHEN Jun. Rechargeable room-temperature Na−CO_2 batteries [J]. Angewandte Chemie (International Edition), 2016, 55(22): 6482−6486.

[15] IM E, RYU J H, BAEK K, MOON G D, KANG S J. "Water-in-salt" and NASICON electrolyte-based Na−CO_2 battery [J]. Energy Storage Materials, 2021, 37: 424−432.

[16] WANG Zhen-zhen, CAI Yi-chao, NI You-xuan, LU Yong, LIN Liu, SUN Hao-xiang, LI Hai-xia, YAN Zhen-hua, ZHAO Qing, CHEN Jun. Ultrafine RuO_2 nanoparticles/MWCNTs cathodes for rechargeable Na−CO_2 batteries with accelerated kinetics of Na_2CO_3 decomposition [J]. Chinese Chemical Letters, 2023, 34(3): 107405.

[17] XU Chang-fan, QIU Jia-jia, DONG Yu-lian, LI Yue-liang, SHEN Yong-long, ZHAO Hua-ping, KAISER U, SHAO Guo-sheng, LEI Yong. Dual-functional electrode promoting dendrite-free and CO_2 utilization enabled high-reversible symmetric Na−CO_2 batteries [J]. Energy Environmental Materials, 2024, 7(3): e12626.

[18] CHEN Xiao-yang, CHEN Jian, LIU Yi-jie, LIU Yang, GAO Yun, FAN Si-wei, HE Xiang-xi, LIU Xiao-hao, SHEN Chao, JIANG Yong, LI Li, QIAO Yun, CHOU Shu-lei. Advanced Li/Na−CO_2 batteries enabled by the γ-MnO_2 catalyst with enhanced carbonate decomposition [J]. ACS Applied Materials & Interfaces, 2023, 15(23): 28106−28115.

[19] THOKA S, TONG Zi-zheng, JENA A, HUNG Tai-feng, WU Ching-chen, CHANG Wen-sheng, WANG Fu-ming, WANG Xing-chun, YIN Li-chang, CHANG Ho, HU Shu-fen, LIU Ru-shi. High-performance Na−CO_2 batteries with $ZnCo_2O_4$@CNT as the cathode catalyst [J]. Journal of Materials Chemistry A, 2020, 8(45): 23974−23982.

[20] PICHAIMUTHU K, JENA A, CHANG Ho, SU Chao-chin, HU Shu-fen, LIU Ru-shi. Molybdenum disulfide/tin disulfide ultrathin nanosheets as cathodes for sodium−carbon dioxide batteries [J]. ACS Applied Materials & Interfaces, 2022, 14(4): 5834−5842.

[21] XU Chang-fan, ZHAN Jing, WANG Zhi-jian, FANG Xin, CHEN Jun, LIANG Feng, ZHAO Hua-ping, LEI Yong. Biomass-derived highly dispersed Co/Co_9S_8 nanoparticles encapsulated in S, N-co-doped hierarchically porous carbon as an efficient catalyst for hybrid Na−CO_2 batteries [J]. Materials Today Energy, 2021, 19: 100594.

[22] DONG Yu-lain, XU Chang-fan, LI Yue-liang, ZHANG Cheng-lin, ZHAO Hua-ping, KAISER U, LEI Yong. Ultrahigh-rate and ultralong-duration sodium storage enabled by sodiation-driven reconfiguration [J]. Advanced Energy Materials, 2023, 13(16): 2204324.

[23] DONG Yu-lian, HUO Jing-yao, XU Chang-fan, JI De-yang, ZHAO Hua-ping, LI Li-qiang, LEI Yong. Research progress on vanadium sulfide anode materials for sodium and potassium-ion batteries [J]. Advanced Materials Technologies, 2024, 9: 2301840.

[24] ZHAN Jing, XU Chang-fan, LONG Yi-yu, LI Qi-hou. Preparation and electrochemical performance of nitrogen-doped carbon-coated $Bi_2Mn_4O_{10}$ anode materials for lithium-ion batteries [J]. Transactions of Nonferrous Metals Society of China, 2020, 30(8): 2188−2199.

[25] MIAO Ze-lin, XU Chang-fan, ZHAN Jing, XU Zi-wei. Morphology-control and template-free fabrication of bimetallic Cu−Ni alloy rods for ethanol electro-oxidation in alkaline media [J]. Journal of Alloys and Compounds, 2021, 855: 157438.

[26] MIAO Ze-lin, ZHAN Jing, XU Zi-wei. Thermodynamic simulation of metal behaviors in Cu^{2+}–Ni^{2+}–NH_3–NH_4^+–$C_2O_4^{2-}$–H_2O system [J]. Transactions of Nonferrous Metals Society of China, 2021, 31(5): 1475−1483.

[27] XU Chang-fan, WANG Huan-wei, ZHAN Jing, KANG Yao, LIANG Feng. Engineering NH_3-induced 1D self-assembly architecture with conductive polymer for advanced hybrid Na−CO_2 batteries via morphology modulation [J]. Journal of Power Sources, 2022, 520: 230909.

[28] FANG Yong-jin, LUAN De-yan, CHEN Ye, GAO Shu-yan, LOU Xiong WEN David. Rationally designed three-layered Cu_2S@Carbon@MoS_2 hierarchical nanoboxes for efficient sodium storage [J]. Angewandte Chemie (International Edition), 2020, 59(18): 7178−7183.

[29] HE Lin, WENIGER F, NEUMANN H, BELLER M S. Synthesis, characterization, and application of metal nanoparticles supported on nitrogen-doped carbon: Catalysis beyond electrochemistry [J]. Angewandte Chemie (International Edition), 2016, 55(41): 12582−12594.

[30] PÉREZ-FONTES S E, PÉREZ-TELLO M, PRIETO-LÓPEZ L O, BROWN F, CASTILLÓN-BARRAZA F. Thermo-analytical study on the oxidation of sulfide minerals at high temperatures [J]. Minerals, Metallurgy & Exploration, 2007, 24(4): 275−283.

[31] GUAN An-xiang, CHEN Zheng, QUAN Yue-li, PENG Chen, WANG Zhi-qiang, SHAM T K, YANG Chao, JI Ya-li, QIAN Lin-ping, XU Xin, ZHENG Geng-feng. Boosting CO_2 electroreduction to CH_4 via tuning neighboring single-copper sites [J]. ACS Energy Letters, 2020, 5(4): 1044−1053.

[32] HUANG Sen-chuan, MENG Yu-ying, HE Shi-man, GOSWAMI A, WU Qi-li, LI Jun-hao, TONG Sheng-fu, ASEFA T, WU Ming-mei. N-, O-, and S-tridopped carbon-encapsulated Co_9S_8 nanomaterials: Efficient bifunctional electrocatalysts for overall water splitting [J]. Advanced Functional Materials, 2017, 27(17): 1606585.

[33] ZHANG Zhen, DENG Ya-ping, XING Zhen-yu, LUO Dan, SY S, CANO Z P, LIU Gui-hua, JIANG Yi, CHEN Zhong-wei. “Ship in a bottle” design of highly efficient bifunctional electrocatalysts for long-lasting rechargeable Zn−air batteries [J]. ACS Nano, 2019, 13(6): 7062−7072.

[34] HUANG Yu-zhu, XING Lin, PEI Shuang, ZHOU Wei, HU Yu-jie, DENG Wei-na, CHEN Liang, ZHU Hai, CHEN Han. Co_9S_8/CNTs microspheres as superior-performance cathodes in aqueous ammonium-ion batteries [J]. Transactions of Nonferrous Metals Society of China, 2023, 33(11): 3452−3464.

[35] HONG Ping, XU Chang-fan, ZHAO Hua-ping, LEI Yong. Atomic size misfit for electrocatalytic small molecule activation [J]. Advanced Functional Materials, 2026, 36: 2502833. https://doi.org/10.1002/adfm.202502833

[36] XU Chang-fan, ZHANG Kai-wen, ZHANG Da, CHANG Shi-lei, LIANG Feng, YAN Peng-fei, YAO Yao-chun, QU Tao, ZHAN Jing, MA Wen-hui, YANG Bing, DAI Yong-nian, SUN Xue-liang. Reversible hybrid sodium−CO_2 batteries with low charging voltage and long-life [J]. Nano Energy, 2020, 68: 104318.

[37] HU Xiao-fei, JOO P H, MATIOS E, WANG Chuan-long, LUO Jian-min, YANG K, LI Wei-yang. Designing an all-solid-state sodium−carbon dioxide battery enabled by nitrogen-doped nanocarbon [J]. Nano Letters, 2020, 20(5): 3620−3626.

[38] LIANG Feng, HAYASHI K. A high-energy-density mixed-aprotic-aqueous sodium−air cell with a ceramic separator and a porous carbon electrode [J]. Journal of the Electrochemical Society, 2015, 162(7): A1215−A1219.

[39] XU Chang-fan, HONG Ping, DONG Yu-lian, LI Yue-liang, SHEN Yong-long, BISKUPEK J, ZHAO Hua-ping, KAISER U, SHAO Guo-sheng, LEI Yong. Multiscale defective interfaces for realizing Na−CO_2 batteries with ultralong lifespan [J]. Advanced Materials, 2024, 36(48): 2409533.

氮掺杂碳包覆 Cu_xS 纳米盒催化剂的制备及其混合系 Na−CO_2 电池的电化学性能

湛 菁[1,2]，华子卓[1]，吴飞翔[1]，李启厚[1]

1. 中南大学 冶金与环境学院，长沙 410083；
2. 新疆工业学院 新能源与矿业学院，和田 848000

摘 要：为了促进混合系钠−二氧化碳(Na−CO_2)电池阴极上 CO_2 的氧化还原动力学，以中空立方 CuS 纳米盒为前驱体，通过吡咯和多巴胺单体的原位聚合并耦合高温热处理得到氮掺杂碳包覆的 $Cu_xS@NC_{PPy}$ 和 $Cu_xS@NC_{PDA}$ 催化剂。结果表明，氮掺杂碳封装不仅增加了材料的比表面积，提高了电子亲和性，而且有效提升了 CuS 活性物种与碳缺陷之间的协同作用，为 CO_2 转化提供了丰富的活性位点。改性的催化剂电化学性能都得到了改善，尤其是基于催化剂 $Cu_xS@NC_{PPy}$ Na−CO_2 电池在 0.1 mA/cm^2 时显示出低的充放电电压差 0.74 V 以及高功率密度 3.42 mW/cm^2。

关键词：CO_2 再利用；硫化铜(I)催化剂；氮掺杂碳；高功率密度；Na−CO_2 电池

(Edited by Xiang-qun LI)